doi:10.1093/brain/awt054 Brain 2013: 136; 1534–1543 | 1534

BRAIN
A JOURNAL OF NEUROLOGY

Exome sequencing reveals mutated *SLC19A3* in patients with an early-infantile, lethal encephalopathy

Sietske H. Kevelam,[1,2] Marianna Bugiani,[1,3] Gajja S. Salomons,[4] Annette Feigenbaum,[5] Susan Blaser,[6] Chitra Prasad,[7] Johannes Häberle,[8] Ivo Barić,[9] Ingrid M. C. Bakker,[2] Nienke L. Postma,[1] Warsha A. Kanhai,[4] Nicole I. Wolf,[1] Truus E. M. Abbink,[1] Quinten Waisfisz,[10] Peter Heutink[2] and Marjo S. van der Knaap[1]

1 Department of Child Neurology, VU University Medical Centre, 1081 HV Amsterdam, The Netherlands
2 Department of Clinical Genetics, Section Medical Genomics, VU University Medical Centre, 1081 HV Amsterdam, The Netherlands
3 Department of Pathology, VU University Medical Centre, 1081 HV Amsterdam, The Netherlands
4 Department of Clinical Chemistry, Metabolic Unit, VU University Medical Centre, 1081 HV Amsterdam, The Netherlands
5 Division of Clinical and Metabolic Genetics, Department of Paediatrics, The Hospital for Sick Children and University of Toronto, Toronto, ON M5G 1X8, Canada
6 Division of Neuroradiology, The Hospital for Sick Children, Toronto, ON M5G 1X8, Canada
7 Department of Paediatrics, Western University Children's Health Research Institute, London, ON N5X 3W2, Canada
8 Division of Metabolism, University Children's Hospital Zurich, CH-8032 Zürich, Switzerland
9 Department of Paediatrics, University Hospital Centre Zagreb and School of Medicine, University of Zagreb, 10000 Zagreb, Croatia
10 Department of Clinical Genetics, VU University Medical Centre, 1081 BT Amsterdam, The Netherlands

Correspondence to: Marjo S. van der Knaap,
Department of Child Neurology,
VU Medical Centre, de Boelelaan 1117,
1081 HV Amsterdam,
The Netherlands
E-mail: ms.vanderknaap@vumc.nl

To accomplish a diagnosis in patients with a rare unclassified disorder is difficult. In this study, we used magnetic resonance imaging pattern recognition analysis to identify patients with the same novel heritable disorder. Whole-exome sequencing was performed to discover the mutated gene. We identified seven patients sharing a previously undescribed magnetic resonance imaging pattern, characterized by initial swelling with T_2 hyperintensity of the basal nuclei, thalami, cerebral white matter and cortex, pons and midbrain, followed by rarefaction or cystic degeneration of the white matter and, eventually, by progressive cerebral, cerebellar and brainstem atrophy. All patients developed a severe encephalopathy with rapid deterioration of neurological functions a few weeks after birth, followed by respiratory failure and death. Lactate was elevated in body fluids and on magnetic resonance spectroscopy in most patients. Whole-exome sequencing in a single patient revealed two predicted pathogenic, heterozygous missense mutations in the *SLC19A3* gene, encoding the second thiamine transporter. Additional predicted pathogenic mutations and deletions were detected by Sanger sequencing in all six other patients. Pathology of brain tissue of two patients demonstrated severe cerebral atrophy and microscopic brain lesions similar to Leigh's syndrome. Although the localization of SLC19A3 expression in brain was similar in the two investigated patients compared to age-matched control subjects, the intensity of the immunoreactivity was increased. Previously published patients with *SLC19A3* mutations have a

Received October 12, 2012. Revised December 22, 2012. Accepted January 25, 2013. Advance Access publication March 12, 2013

milder clinical phenotype, no laboratory evidence of mitochondrial dysfunction and more limited lesions on magnetic resonance imaging. In some, cerebral atrophy has been reported. The identification of this new, severe, lethal phenotype characterized by subtotal brain degeneration broadens the phenotypic spectrum of *SLC19A3* mutations. Recognition of the associated magnetic resonance imaging pattern allows a fast diagnosis in affected infants.

Keywords: early infantile encephalopathy; magnetic resonance imaging; *SLC19A3*

Introduction

Early-infantile onset encephalopathies have a major impact on families. They come with an urgent need for a proper diagnosis in view of immediate therapeutic decisions. Additionally, the diagnosis is important for genetic counselling and family planning. MRI pattern recognition has been proven to be highly successful in facilitating a rapid correct classification and diagnosis (Schiffmann and van der Knaap, 2009). Several novel childhood encephalopathies have been defined by their distinct pattern of MRI abnormalities and in most cases the aetiology has been identified, confirming the validity of this approach (Leegwater *et al*., 2001*a*, *b*; Zara *et al*., 2006; Scheper *et al*., 2007; Steenweg *et al*., 2012*a*, *b*). Most of these disorders have a genetic aetiology with a Mendelian inheritance pattern. Different genetic techniques, including genome-wide linkage studies and homozygosity mapping, have been used to identify the associated genes (Leegwater *et al*., 2001*a*, *b*; Zara *et al*., 2006; Scheper *et al*., 2007). Although successful for common Mendelian disorders and large or consanguineous families, these conventional techniques fail to elucidate the related gene in extremely rare Mendelian disorders, unrelated cases from different families, and sporadic cases owing to *de novo* mutations. The recent introduction of whole-exome sequencing has created the opportunity to identify the mutated gene in these cases leading to rapid new gene discoveries (Ku *et al*., 2011; Steenweg *et al*., 2012*a*, *b*). In the present study we used MRI pattern recognition for the classification of a group of seven patients with a lethal encephalopathy of unknown origin and performed whole-exome sequencing as a first-tier genetic technique to identify the related gene.

Patients and methods

Seven patients from five unrelated families, sharing a previously undescribed distinct MRI pattern, were identified from our MRI database of more than 3000 cases with an unclassified leukoencephalopathy. Patients were included if they met the following MRI criteria: (i) bilateral signal abnormalities of the nucleus caudatus, putamen, globus pallidus and thalamus; (ii) extensive signal abnormalities of the subcortical and central cerebral white matter and the cerebral cortex; (iii) diffuse signal abnormalities of the cerebellar white matter with or without involvement of the cortex; (iv) extensive signal abnormalities in the pons and midbrain; and (v) in the case of follow-up MRIs, atrophy of affected structures.

Detailed clinical information, laboratory investigations and autopsy results were retrospectively collected and reviewed. A molecular diagnosis was not achieved in any of the patients. Blood and/or fibroblasts of all patients were collected. Approval of the ethical standards committee was received for whole-exome sequencing in patients with unclassified leukoencephalopathies, with written informed consent of the parents.

Magnetic resonance imaging pattern recognition

A total number of 15 MRIs were available for the study. MRIs were evaluated according to a previously published protocol by consensus of two investigators (S.H.K. and M.S.v.d.K.) (van der Knaap *et al*., 1999). Studies typically included sagittal T_1-weighted spin-echo images and axial T_1-weighted, T_2-weighted and proton density spin-echo images. FLAIR images were available in six patients. Signal changes were defined as abnormally high signals on T_2-weighted images. White matter rarefaction was defined as T_2-hyperintense white matter areas with low signal on FLAIR or proton density, but not as low as the signal CSF. Cystic degeneration was defined as T_2-hyperintense white matter areas with a low signal on FLAIR or proton densitiy, as low as the signal of CSF. Cerebral atrophy was scored as mild, moderate or severe, based on the presence of cerebral or cerebellar sulcal prominence, enlargement of the ventricles and subjective assessment of brainstem size. Apparent diffusion coefficient maps were used to assess restricted diffusion to avoid the T_2-shinethrough effects. Because magnetic resonance spectroscopy studies were obtained with different techniques on machines from different vendors, we only looked at the presence of lactate, represented by a doublet centred at 1.33 parts per million. The MRIs of four disease stages (acute, post-acute, intermediate and end-stage) were grouped together.

Whole-exome sequencing

Whole-exome sequencing was performed in Patient 2. Genomic DNA was extracted by standard methods. Exonic targets were enriched with SeqCap EZ Human Exome Library v2.0 kit (Nimblegen). Sequencing was performed with 100 bp paired-end reads on a Hiseq2000 (Illumina). Read alignment to the human genome assembly hg19 was performed with Burrows-Wheeler Aligner tool (v0.5.9) (http://bio-bwa.sourceforge.net) (Li and Durbin, 2009). Single-nucleotide variants and small insertions and deletions were called with Varscan v2.2.5 (http://varscan.sourceforge.net) (Koboldt *et al*., 2009) and annotated with Annovar (http://www.openbioinformatics.org/annovar) (Wang *et al*., 2010). Novelty of variants was determined using public single nucleotide polymorphism databases, including dbSNP132 (http://www.ncbi.nlm.nih.gov/projects/SNP) and the 1000 Genomes project (release November 2010), and our in-house control exomes (yielding 17 exomes of patients with different disease phenotypes). PolyPhen-2 was used for pathogenicity prediction of variants (http://genetics.bwh.harvard.edu/pph2/) (Adzhubei *et al*., 2010).

Mutation analysis

All coding exons and the adjacent splice sites of the *SLC19A3* gene of the index patients were amplified by PCR (NG_016359.1). For one case the full length open reading frame was amplified by reverse-transcription PCR (NM_025243.3). The DNA of parents was only investigated for the amplicons containing the familial mutations. All *SLC19A3* amplicons were analysed by direct DNA sequence analysis. The amplicons were analysed by capillary electrophoresis using an ABI3130xl genetic analyser (Applied Biosystems) and assessed using Mutation Surveyor® (Softgenetics). Primer sequences are available on request.

Pathology

Brain tissue from Patients 3 and 4 was collected at autopsy at The Hospital for Sick Children, Toronto, Ontario, Canada. Macroscopic and microscopic characteristics and the expression patterns of SLC19A3 and SLC19A2 were studied. To investigate the normal expression of SLC19A3 and SLC19A2, post-mortem brain tissue samples were obtained from four unrelated age-matched control subjects without significant confounding neuropathological findings at autopsy and from one 2-year-old child with Leigh's syndrome. Leigh's syndrome was diagnosed based on the clinical course, the typical MRI pattern and pathology findings of Leigh's syndrome at autopsy. No molecular diagnosis was achieved. Formalin-fixed, paraffin-embedded tissue was sectioned at 6 μm and stained for haematoxylin and eosin or Kluver-periodic acid Schiff according to standard methods. Additionally, tissue sections were incubated with antibodies against the following epitopes: SLC19A3 (Sigma, 1:500) and SLC19A2 (Sigma, 1:100), glial fibrillary acidic protein (GFAP, marker of astrocytes; Millipore, 1:1000), proteolipid protein (PLP, myelin marker; AbDSerotec, 1:3000), neuronal nuclear antigen (NeuN, marker of neurons; Sigma, 1:500), platelet endothelial cell adhesion molecule 1 (PECAM1/CD31, vascular endothelial cell marker; Dako, 1:50), and collagen IV (basement membrane marker; Dako, 1:50). Negative controls by omitting the primary antibody were included in each experiment to verify the specificity of the immunohistochemical labelling. Briefly, sections were deparaffinized and rehydrated. Endogenous peroxidase activity was quenched by incubating the slides in 0.3% hydrogen peroxide in methanol. Slides were rinsed with distilled water and transferred to citric acid (pH 6). Heat-induced antigen retrieval was performed using microwave irradiation for 15 min on low setting. Tissue sections were then cooled to room temperature, rinsed and incubated overnight with primary antibodies. Slides were rinsed and the antibody visualized with diaminobenzidine tetrachloride. Between incubation steps, sections were thoroughly washed. After a short rinse in tap water, sections were counterstained with haematoxylin, washed, dehydrated and mounted with polyvinyl alcohol medium with Dabco® (Sigma).

Double and triple fluorescence immunohistochemical stainings were performed on cryosections of snap-frozen brain tissue from the same control subjects. Tissue sections were fixed in 2% paraformaldehyde, subsequently permeabilized with 0.1% saponin, blocked in 5% normal goat serum and incubated with primary antibodies overnight at 4°C. After staining with secondary antibodies (Alexa Fluor® 488-, 568-, and 647-tagged; Molecular Probes, 1:400), sections were counterstained with DAPI (nuclear stain; Molecular Probes, 10 ng/ml) and photographed using a Leica DM6000B microscope (Leica Microsystems).

Results

Magnetic resonance imaging findings

Detailed MRI findings are outlined in Supplementary Table 1. Most patients had more than one brain MRI; only Patients 1 and 2 had a single MRI. Four follow-up MRIs were available in Patient 5, illustrating all four disease stages (Supplementary Fig. 1).

The acute phase (MRI of two patients, Supplementary Table 1; Fig. 1A–C, Patient 1) was characterized by severe swelling and diffuse T_2-hyperintensity of the cerebral and cerebellar white matter and cortex. Typically, the depths of the sulci of the cerebral and cerebellar cortex were affected, with a high T_2-signal, while the gyral crowns had a more normal, low T_2-signal. Severe swelling and T_2-hyperintensity of central grey nuclei, including the thalamus, putamen, globus pallidus, caudate nucleus and dentate nucleus were present in both patients. The brainstem displayed extensive signal abnormalities with relative sparing of the medulla oblongata. Rarefaction of the deep cerebral white matter was seen in Patient 1. Diffusion imaging of Patient 5 showed restricted diffusion in multiple areas of the cerebral cortex and white matter, corpus callosum, basal nuclei, thalamus, brainstem, and cerebellar white matter.

The post-acute phase (MRI of three patients, Supplementary Table 1; Fig. 2A–F, Patient 6) was characterized by partial resolution of cerebral white matter swelling with rarefaction and/or cystic degeneration of predominantly the subcortical white matter, the basal nuclei and thalamus. The pulvinar was relatively spared in Patients 6 and 7. Diffusion imaging was performed in Patient 6 and revealed extensive areas of restricted diffusion in cerebral white and grey matter structures (Fig. 2D and E). The widespread signal abnormalities of midbrain and pons persisted in all patients and new signal abnormalities of the medulla oblongata developed in Patient 5.

The intermediate phase (MRI of six patients, Supplementary Table 1; Fig. 3A–C; Patient 3) consisted of a variable degree of atrophy of the brainstem, thalami, basal nuclei, cerebral white matter and corpus callosum, accompanied by extensive thinning of the cerebral cortex. Rarefaction of cerebral and/or cerebellar white matter was present in three of the six patients. Cyst-like structures were present throughout the cerebral white matter, the thalami, basal nuclei, and cerebellar white matter in two patients. Although the widespread T_2-hyperintensity of the brainstem decreased, focal T_2-signal abnormalities localized in the central-dorsal area of the tegmentum of pons and midbrain persisted. Previously detected areas of restricted diffusion resolved. A subdural haematoma developed in three patients, most likely due to advancing cerebral atrophy.

The end stage (MRI of five patients, Supplementary Table 1; Fig. 4A–C, Patient 4) was characterized by severe atrophy of the cerebral white matter and cortex, corpus callosum, thalami and basal nuclei. Cerebellar atrophy was noted in three patients. Atrophy of the pons and midbrain with persisting T_2-hyperintensity of the central-dorsal area of the tegmentum of pons and midbrain was present in four patients.

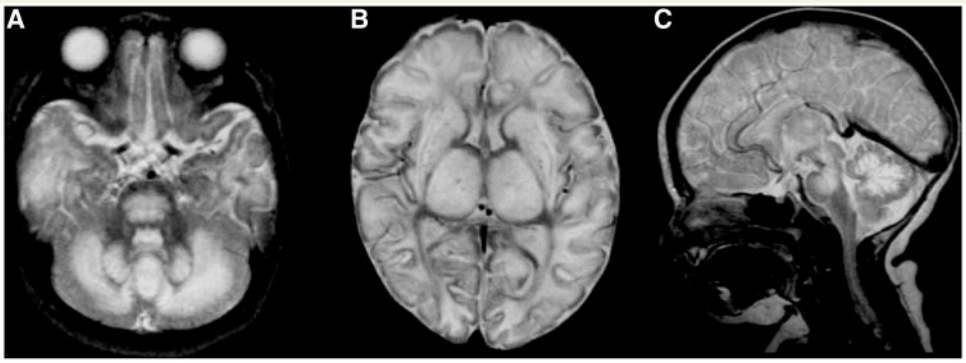

Figure 1 Axial (**A** and **B**) and sagittal (**C**) T_2-weighted images in Patient 1 at 3 months of age, illustrating the acute phase. Note the extensive swelling and T_2-hyperintensity of the cerebral and cerebellar white matter, basal nuclei and thalami (**B**). The depths of the gyri of the cerebral and cerebellar cortex are more affected than the gyral crowns (**B** and **C**).

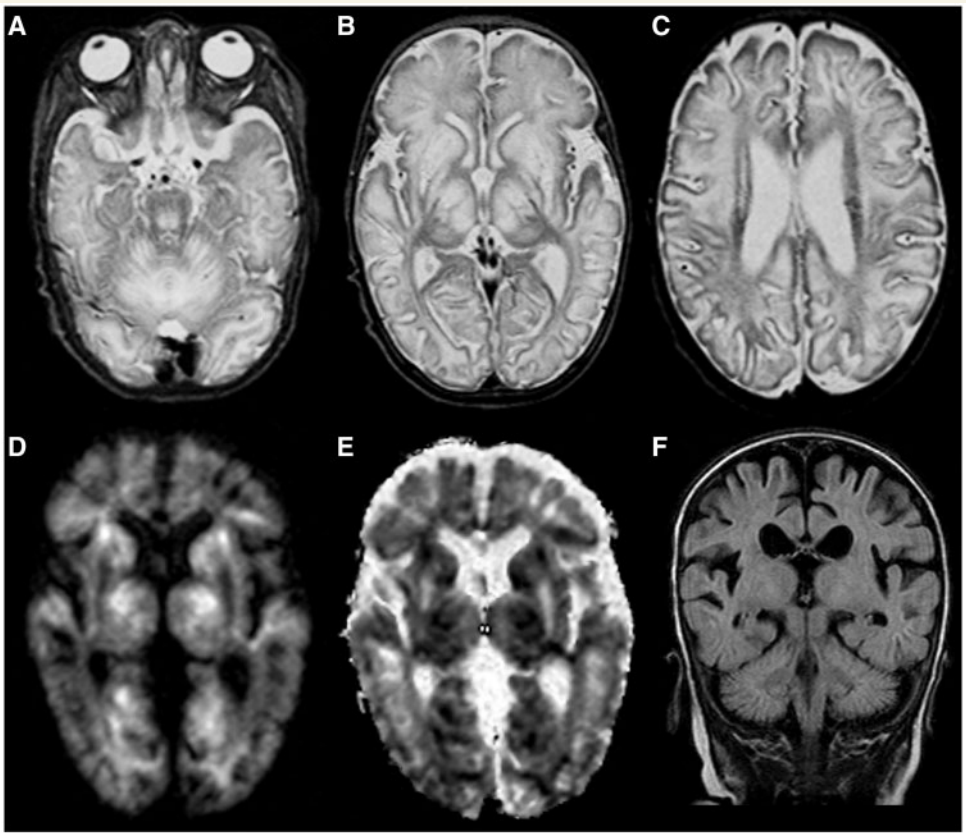

Figure 2 Axial T_2-weighted images (**A–C**), diffusion-weighted images (**D** and **E**), and a coronal FLAIR image (**F**) in Patient 6 at 2.9 months of age, illustrating the post-acute phase. Moderate swelling of the cerebral white matter, basal nuclei and thalami is observed (**B** and **C**). Note the relative sparing of the pulvinar (**B**). There is restricted diffusion in the thalami, caudate nucleus and different parts of the cerebral white matter (**D** and **E**). Multiple areas of rarefied white matter are present (**F**).

Elevated lactate in affected white and grey matter was found by magnetic resonance spectroscopy in five patients during one or more disease stages (Supplementary Table 1). Contrast was given to Patients 6 and 7 during the post-acute phase, and to Patient 5 during the intermediate phase. No enhancement was observed. It is important to note that the four disease stages followed each other rapidly and that the brain abnormalities evolved in the course of a few weeks to months.

Clinical findings

Detailed clinical characteristics and findings at last examination are described in Supplementary Table 2. Patients 2 and 4,

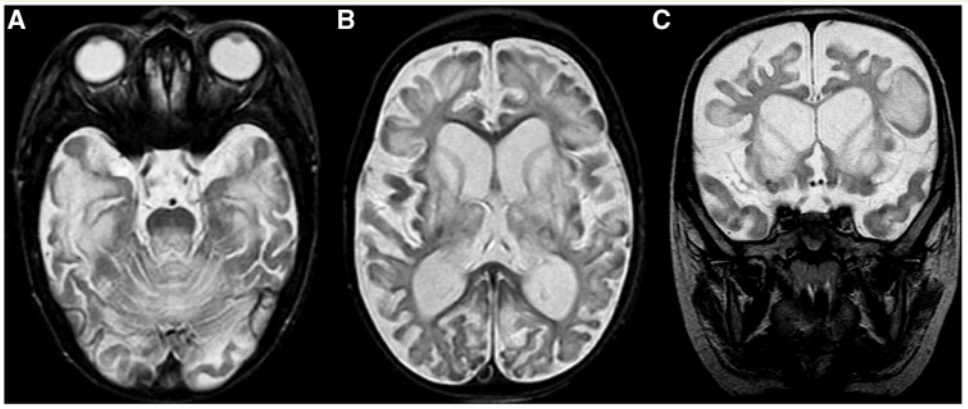

Figure 3 Axial (**A** and **B**) and coronal (**C**) T_2-weighted images in Patient 3 at 2.3 months of age, illustrating the intermediate phase. Note the atrophy of the cerebral white matter and thinning of the cortex (**B** and **C**). Cystic lesions of the basal nuclei, thalami and subcortical white matter are present (**B** and **C**). The T_2-hyperintensity of the pons is restricted to the central-dorsal area (**A**).

as well as Patients 5 and 7 are siblings. Consanguinity was present in two families. Pregnancy and delivery were uneventful for all patients. Early psychomotor development was delayed in the siblings Patients 5 and 7. The initial signs were noted between 8 weeks and 5.5 months of age (mean 2.7 months) and included irritability, seizures or suspected seizures, sometimes infantile spasms, loss of contact, somnolence and lowering of consciousness, extensor spasms, feeding difficulties and failure of achieving developmental milestones. A preceding event was evident in six patients, including (viral) infection or vaccination shortly before onset. Within a few weeks after the first signs, all patients showed rapid and severe regression of neurological functions with progressive spasticity, deterioration of contact, feeding difficulties, and eventually respiratory failure. Six patients died before the age of 2 years (range 4–20 months); Patient 6 died at the age of 4 years and 8 months. Neurological examination predominantly showed pyramidal signs of arms and legs; no extrapyramidal signs were present. Ophthalmological investigation revealed optic nerve atrophy in most patients. None of the seven patients had involvement of other organs or dysmorphic features. Patients 1 and 3 received a 'mitochondrial' cocktail, including vitamin B6, co-enzyme Q, riboflavin, nicotinamide, and biotin, but no thiamine. No beneficial effect of the supplements was observed.

Laboratory findings

Laboratory findings are summarized in Supplementary Table 3. Plasma lactate levels were elevated in five patients at initial presentation (range 3.3–4.6 mmol/l, normal values 1.2–2.2 mmol/l) and showed a subsequent gradual decline during follow-up. Amino acid levels in blood revealed a slightly elevated alanine in three patients with increased ornithine and glycine in one patient. Plasma thiamine levels were not measured. Urinary organic acids were normal in all patients. A slightly reduced activity of one or more respiratory chain enzyme complexes in muscle was found in three patients. However, normal enzyme activities were measured in skin fibroblasts. Ragged red fibres or structural mitochondrial abnormalities were not observed. Mutation analysis of whole mitochondrial DNA in blood or targeted mutation analysis of mitochondrial DNA in muscle or blood revealed no mutations in the tested patients.

Whole-exome analysis

Whole-exome sequencing was performed in DNA of Patient 2. To prioritize candidate disease genes, we filtered the raw data based on the assumptions that the causal variant was not present in control exomes, was compliant with an autosomal recessive inheritance and altered the amino acid sequence, as summarized in Supplementary Table 4. This approach selected three genes with variants fulfilling these criteria: *SLC19A3 (*MIM*606152), *SLC34A1* (MIM*182309) and *OBSL1* (MIM*610991). Based on conservation status, predicted pathogenicity using Polyphen-2 (Adzhubei *et al*., 2010) and a literature search for disease phenotypes linked to these genes, we selected *SLC19A3* as the best candidate gene. The two heterozygous *SLC19A3* variants detected in Patient 2, a c.541T>C transition predicting the replacement of serine at protein position 181 by proline p.Ser181Pro and a c.1154T>G transversion predicting a p.Leu385Arg replacement, were confirmed by Sanger sequencing. DNA from the parents was not available to confirm compound heterozygosity.

SLC19A3 mutation analysis

Sanger sequencing of *SLC19A3* identified missense and nonsense mutations and deletions in all seven patients (Table 1). Except for Patients 5 and 7, no DNA from parents was available so carrier status in the parents could not be confirmed. All identified mutations were not present in 13 000 control chromosomes of subjects included in the NHLBI GO Exome Sequencing Project database and were predicted to be probably pathogenic by Polyphen-2 (Adzhubei *et al*., 2010) (Table 1). Patient 1 harboured the p.Gly23Val mutation on one allele, which was previously found in homozygous state in two patients from a Yemeni

family with biotin-responsive basal ganglia disease (Zeng *et al.*, 2005).

Brain pathology

Macroscopic examination of the brain of Patients 3 and 4 showed severe atrophy of the cerebral cortex, deep grey matter structures and subcortical and central white matter. Microscopic examination confirmed the involvement of both grey and white matter with multiple, bilateral and often symmetric infarct-like lesions in the cerebrum, brainstem (Fig. 5G) and cerebellum. All lesions were characterized by rarefaction and vacuolar degeneration to cavitary necrosis of the neuropil and surrounding white matter, accompanied by prominent, dilated capillaries and reactive astrogliosis (Fig. 5A–D). In the cerebral and cerebellar cortex these lesions affected preferentially the depth of the sulci and extended to the pial surface (Fig. 5E and F). Here subtotal loss of neurons was associated with infiltration of lipid-laden macrophages and mineralization of the residual neurons (Fig. 5B). The lesions in the basal nuclei (Fig. 5D), brainstem and cerebellum had the same histopathological features. Notably, well-preserved neurons in the context of nectrotizing areas were found in the midbrain and pontine tegmentum (Fig. 5H). Although relatively spared, the deep white matter also showed myelin pallor, microcystic changes, dilated perivascular spaces, and marked isomorphic reactive astrogliosis (data not shown).

In the non-neurological controls, SLC19A2 and SLC19A3 were expressed in the blood vessels throughout the brain (Fig. 6A and B). Double labelling showed co-localization of SLC19A3 with collagen IV at the basement membrane and in the surrounding pericytes (Supplementary Fig. 2A). By contrast, SLC19A2 immunoreactivity was found only at the luminal side of the blood vessels, where it co-localized with the endothelial marker CD31 (Supplementary Fig. 2D). In the control cerebral cortex, SLC19A3 expression was also found in meningeal cells and in some NeuN-positive small neurons in the deeper cortical layers (Supplementary Fig. 2F) and immediately subcortical cerebral white matter (Fig. 6A). Scattered SLC19A3-positive neurons were also seen in the brainstem and cerebellar nuclei. No SLC19A3 expression was seen in astrocytes (Fig. 6A; Supplementary Fig. 2E and F). No other SLC19A2-positive cell types beside blood cells were seen in the cerebral cortex (data

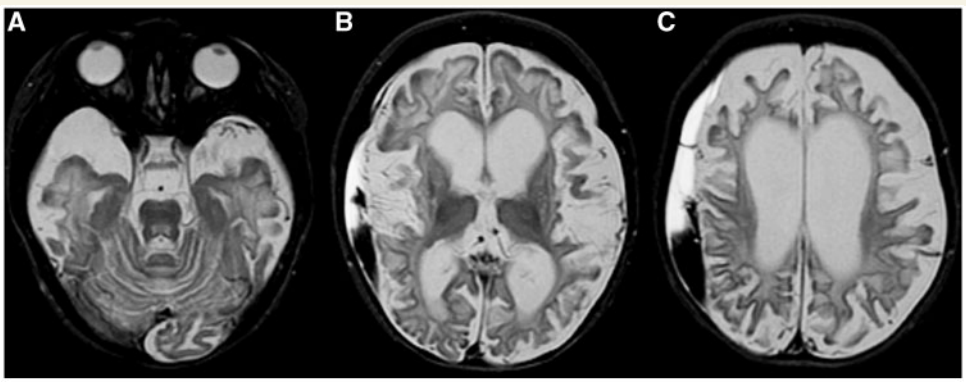

Figure 4 Axial T_2-weighted images in Patient 4 at 9.5 months of age, illustrating the end phase. Note the advanced atrophy of the cerebral white matter, basal nuclei, thalami and cortex (**A–C**). The signal abnormalities of the pons have almost completely disappeared (**A**).

Table 1 ***SLC19A3*** **mutations in present patients**

Patient	Country of origin	c.DNA	Deduced effect[a]	Type of mutation	State	Exon
1	Canadian	c.68G>T[b]	p.Gly23Val[b]	Missense	Heterozygous	2
		r.1173_1314del	p.Gln393*	Exon deletion	Heterozygous	5
2 and 4 (sibs)	European	c.541T>C	p.Ser181Pro	Missense	Heterozygous	3
		c.1154T>G	p.Leu385Arg	Missense	Heterozygous	4
3	European	c.507C>G	p.Tyr169*	Nonsense	Heterozygous	3
		c.527C>A	p.Ser176Tyr	Missense	Heterozygous	3
5 and 7 (sibs)	Lebanese	c.895_925del	p.Val299fs	Frameshift	Homozygous[c]	3
6	Moroccan	c.1332C>G	p.Ser444Arg	Missense	Homozygous	6

The missense mutations described are presumed to be pathogenic, because all mutations have been analysed with Polyphen-2 and had prediction scores $\geqslant$0.92, the amino acids involved are all moderately to highly conserved, and none of the mutations were detected in $\geqslant$13 000 control alleles. However, to confirm pathogenicity, overexpression studies need to be performed. All other type of mutations detected in this study should be considered pathogenic based on their truncating nature.

[a] Nomenclature rules of den Dunnen and Antonarakis (2001).

[b] Known mutation (Zeng *et al.*, 2005).

[c] Both parents are carrier of the mutation, confirming homozygosity for the mutation in their affected children.

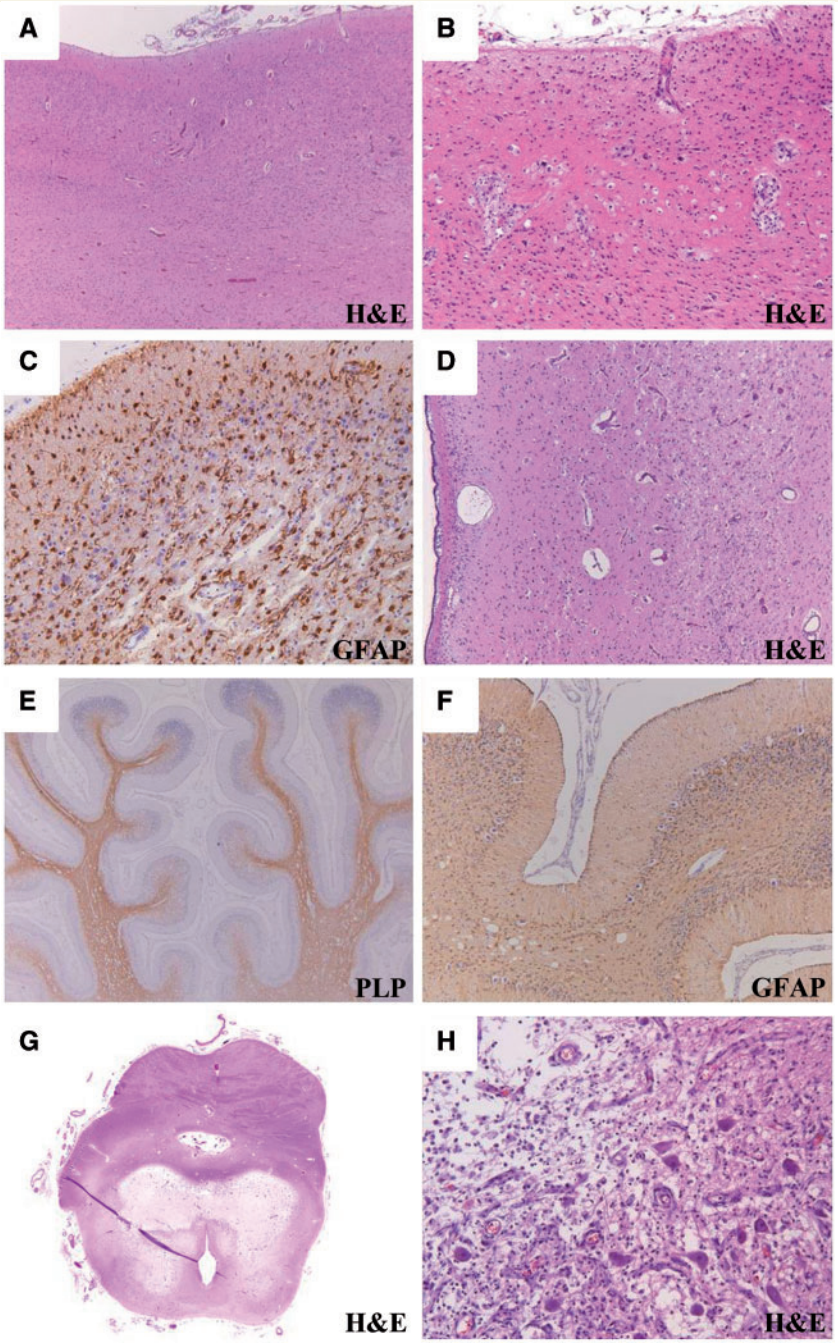

Figure 5 Haematoxylin and eosin (H&E) stain of the cerebral cortex shows an infarct-like lesion extending to the pial surface and to the subcortical white matter (**A**, Patient 4). Note the relatively spared cortex on the left side of the picture. At higher magnification lesions display rarefaction and loosening of the neuropil with subtotal loss of neurons, lipophages and chronic fibrillary astrogliosis (**B**, Patient 4). Immunolabelling for glial fibrillary acidic protein (GFAP) shows marked reactive proliferation of astroglial cells (**C**, Patient 4). Haematoxylin and eosin stain of the basal nuclei shows rarefaction of the neuropil with vascular prominence in the putamen (**D**, Patient 4). Immunostain for the proteolipid protein (PLP) shows white matter rarefaction with loss of stainable myelin deeper in the folia. Note also the moderate cortical atrophy and the relative sparing of the cortex at the crowns of the gyri, with still visible external and internal granular layers (**E**, Patient 3). Immunolabelling for glial fibrillary acidic protein from the same patient shows reactive proliferation of the white matter astrocytes and of the Bergmann glia. Note also the total loss of neurons in the depth of the gyri, including the Purkinje cells (**F**, Patient 3). Whole mount of haematoxylin and eosin-stained cross section through the pontomesencephalic junction shows bilaterally symmetric necrotizing lesions in the tectum and tegmentum with relative sparing of the peri-aqueductal areas. Note the presence of an additional midline necrotizing lesion in the raphe (**G**, Patient 4). Haematoxylin and eosin stain of the oculomotor nucleus (III cranial nerve) in the midbrain shows marked rarefaction to liquefaction of the neuropil with astrogliosis, lipophages, dilated blood vessels and relative sparing of some neuronal cells (**H**, Patient 3).

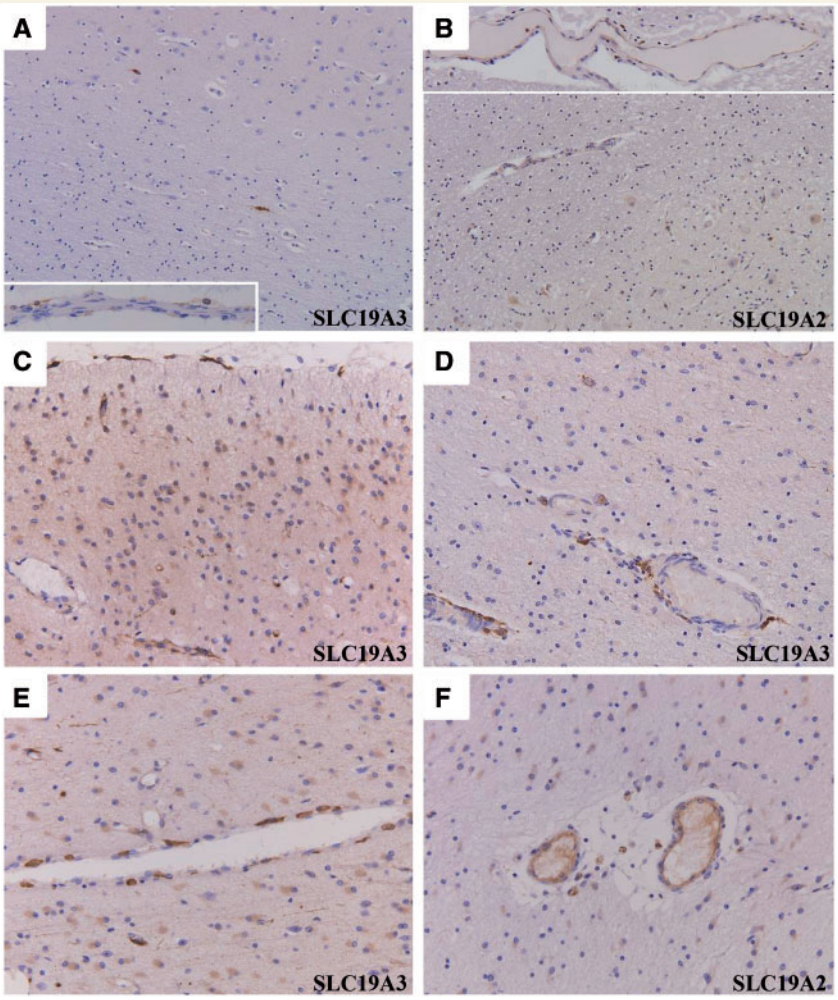

Figure 6 Stain for SLC19A3 in control brain tissue shows scattered strongly immunoreactive neurons in the deeper cerebral cortex (*top right*) and corticosubcortical junction (**A**). SLC19A3-immunoreactivity is also visible in the wall of blood vessels (**A**, *inset*) along the basement membrane and in pericytes. Stain for SLC19A2 of the cerebellar white matter shows immunopositivity of the vascular endothelial cells (**B**, *inset*). Note also a faint immunoreactivity in the neurons of the dentate nucleus (**B**). Labelling for SLC19A3 of a cortical lesion from Patient 4 shows increased immunoreactivity at the blood vessel walls and immunopositive parenchymal and subpial astrocytes (**C**). A similar constellation of findings is visible in a grey matter lesion from the age-matched control with Leigh's encephalopathy unrelated to SLC19A3. Note the apparent less pronounced SLC19A3-immunoreactivity in the reactive astrocytes (**D**). Stain for SLC19A3 of a relatively spared subcortical white matter area in the frontal lobe of Patient 4 shows strong immunoreactivity in the perivascular pericytes and, to a lesser extent, in the reactive astrocytes (**E**). Labelling for SLC19A2 of the same brain region of the same patient shows increased immunopositivity in the vascular endothelial cells and reactive astrocytes (**F**).

not shown), whereas scattered faintly SLC19A2-positive neurons were visible in the deep cerebellar nuclei (Fig. 6B) and in the brainstem.

In the two *SLC19A3*-mutated patients, as well as in the patient with Leigh's syndrome, a stronger immunoreactivity for both SLC19A3 and, to a lesser degree, SLC19A2 was detected in the wall of the blood vessels (Fig. 6C–F). The localization of both transporters was the same as in normal control tissue. In contrast with non-neurological controls, numerous SLC19A3-positive astrocytes were also seen in and around infarct-like lesions in the *SLC19A3*-mutated patients (Fig. 6C and E) and, to a lesser degree, in the patient with Leigh's syndrome (Fig. 6D). Increased SLC19A3 expression was also detected in subpial astrocytes (Fig. 6C).

Discussion

Using MRI pattern recognition we identified a group of young infants with a dramatic, lethal encephalopathy with subtotal brain degeneration. Exome sequencing of one patient and subsequent Sanger sequencing of six patients revealed (presumed) pathogenic mutations in the *SLC19A3* gene. *SLC19A3* encodes the second thiamine transporter and is ubiquitously expressed, including in brain (Rajgopal *et al*., 2001).

The cerebral MRI abnormalities of our patients indicate rapid onset and massive neuronal cell death, suggestive of severe energy failure. The white matter abnormalities can be explained by Wallerian degeneration. Different disease phases follow each other rapidly and soon lead to subtotal brain degeneration. Initial

diffuse swelling with T_2-hyperintensity of the cerebral cortex and white matter, caudate nucleus, putamen, globus pallidus, thalami, dentate nucleus, cerebellum, pons and midbrain is followed by rarefaction and cystic degeneration of the white matter and progressive cerebral, cerebellar and brainstem atrophy. Deficiency of thiamine pyrophosphate, the active form of thiamine, can explain this energy failure due to its important role as cofactor for three major enzyme systems involved in the tricarboxylic acid cycle. The developing brain is a large energy consumer and can therefore be regarded as one of the most vulnerable organs for thiamine deficiency.

Parallel to the rapidly progressive MRI abnormalities, patients deteriorate dramatically within a few weeks after the first signs and die early. In the majority of the patients the onset of deterioration was preceded by an infection or vaccination, a feature also commonly seen in mitochondrial disorders. Most patients have elevated lactate levels in plasma and on spectroscopy. These findings are consistent with the hypothesis that thiamine deficiency leads to decreased oxidative decarboxylation of pyruvate and α-ketoglutarate acid, resulting in pyruvate accumulation and lactate production (Jhala and Hazell, 2011).

In our patients, brain pathology shows symmetric, bilateral infarct-like lesions with profound loss of neurons, astrogliosis and vascular prominence, comparable to what is observed in Leigh's syndrome (Powers and de Vivo, 2002). The observation that the crowns of the gyri are less severely affected than the depth of the sulci, as seen both by brain MRI and histologically, is a typical finding in conditions of energy failure (van der Knaap and Valk, 2005). The pathological findings in our patients are, however, more severe and extensive than commonly observed in patients with Leigh's syndrome (Powers and de Vivo, 2002).

The expression of SLC19A3 and SLC19A2 has been extensively studied in intestinal and renal epithelial cells (Said *et al*., 2004; Ashokkumar *et al*., 2006), but not in the brain. In our study, we found that both wild-type transporters are differentially expressed within cerebral blood vessels. SLC19A2 is expressed exclusively at the luminal side, while SLC19A3 is solely present at the basement membrane and in perivascular pericytes. This distribution differs from that observed in intestinal and renal epithelial cells, where SLC19A3 is present at the luminal apical side and SLC19A2 at both the luminal and baso-lateral side (Said *et al*., 2004; Ashokkumar *et al*., 2006). This differential distribution could indicate a different role of both thiamine transporters in thiamine homeostasis. Because the localization of both transporters in the brain is different than observed in renal and intestinal tissue, regulation of thiamine homeostasis could be different for these organs.

Compared with non-neurological controls, both transporters locate to the same position in cerebral blood vessels of the two *SLC19A3*-mutated patients investigated histopathologically. However, their expression is increased. The observation that their expression is also increased in the patient with Leigh's syndrome may imply that the upregulation of the thiamine transporters is not the direct consequence of decreased intracellular thiamine, but of decreased energy availability. In the two investigated *SLC19A3*-mutated patients, however, SLC19A3 and SLC19A2 expression was detected in reactive astrocytes to a greater degree than in the patient with Leigh's syndrome. This suggests that the intracellular thiamine level affects the expression of both transporters in this cell type. The increased SLC19A3 and SLC19A2 expression is possibly due to a regulatory feedback mechanism. We could not determine whether this is specific for the brain or also concerns the thiamine transporters located in other organs, like the intestine and the kidney, because no intestinal or renal material from patients was available in which we could investigate the expression of the transporters. Plasma thiamine levels were not measured, so it remains unknown if thiamine absorption in the intestine or kidney is affected in these patients. It also remains to be investigated whether increased brain SLC19A3 and SLC19A2 expression is a general feature observed in patients with *SLC19A3* mutations.

Until now, *SLC19A3* mutations have been associated with three different clinical variants (see Supplementary Table 5 for an overview of all patients reported with *SLC19A3* mutations): basal ganglia disease (MIM#607483), Wernicke-like encephalopathy (MIM#607483) and a more generalized encephalopathy (Zeng *et al*., 2005; Kono *et al*., 2009; Debs *et al*., 2010; Yamada *et al*., 2010; Serrano *et al*., 2012). Patients with basal ganglia disease have a childhood or adolescent onset encephalopathy, mainly characterized by epilepsy, confusion, dysarthria, dysphagia and extrapyramidal symptoms. MRI shows focal lesions predominantly in the putamen and caudate nucleus. Patients improve on biotin or thiamine medication (Zeng *et al*., 2005; Debs *et al*., 2010; Serrano *et al*., 2012). Patients with Wernicke-like encephalopathy have an adolescent onset encephalopathy, clinically resembling Wernicke syndrome. MRI also shows the typical abnormalities involving the peri-aqueductal grey and medial thalamus. These patients improved on thiamine medication (Kono *et al*., 2009). The patients with the more generalized encephalopathy have an infantile onset and a more severe phenotype, characterized by infantile spasms and psychomotor retardation. Besides focal lesions in the basal nuclei, their brain MRI also shows cerebral atrophy (Yamada *et al*., 2010). The effect of biotin or thiamine could not be determined in the latter patients. Overall, these three phenotypes have a milder clinical course and a different MRI pattern with more limited abnormalities than our patients. Elevated lactate levels as evidence of mitochondrial dysfunction were not reported in any of these cases.

We identified different heterozygous or homozygous missense and nonsense mutations and deletions in *SLC19A3* in our patients. All mutations identified were novel, except for the heterozygous p.Gly23Val mutation in Patient 1 (on the other allele this patient had a deletion of 141 base pairs). This mutation was previously found in homozygous state in two patients from one family with basal ganglia disease (Zeng *et al*., 2005). Owing to the small number of patients known, a clear genotype–phenotype relationship cannot be established. The consistent phenotype in multiple affected siblings, however, suggests that the genotype indeed influences the phenotype. It could be that patients with a milder phenotype are less vulnerable to thiamine deficiency due to some remaining function of the mutant protein or due to individual genetic or epigenetic factors, for instance positively influencing the expression of SLC19A2 or RFC1, a potential thiamine monophosphate transporter (Zhao *et al*., 2001, 2002).

Our findings broaden the phenotypic spectrum of patients with *SLC19A3* mutations. The cause of the clinical heterogeneity associated with mutated *SLC19A3* remains to be elucidated. Recognition of the distinctive MRI pattern associated with the different clinical phenotypes is important as it allows a rapid diagnosis in affected infants. Regarding treatment possibilities, two of our patients received biotin, without thiamine, and had no signs of improvements. The problem with this severe phenotype is that the brain damage is already extensive when patients come to medical attention. At present, the most important implication of the diagnosis for families is in genetic counselling and prenatal diagnosis. Whether antenatal supplementation of thiamine and biotin has any beneficial effect remains to be investigated.

Acknowledgements

We would like to thank the families for their cooperation with our study, and colleagues caring for the patients for their contributions. We thank Dr. Glenn Taylor and Susan Cromwell, Paediatric Laboratory Medicine, The Hospital for Sick Children, Toronto, Canada, for generously providing the brain tissue. We thank Dr. C. Anthony Rupar, Director, Biochemical Genetics Laboratory, London Health Sciences Centre, London, Ontario, Canada for his contributions to the biochemical analyses. We are grateful to Silvy van Dooren, Department of Clinical Chemistry, Metabolic Unit, VU University Medical Centre, Amsterdam, the Netherlands, for her assistance in the Sanger sequence analysis. We thank Dr. Gabriele Wohlrab, department of child neurology, Kinderspital, Zurich, Switzerland for referral of one of the patients.

Funding

The study received financial support from ZonMw TOP grant 91211005 and the Optimix Foundation for Scientific Research.

Supplementary material

Supplementary material is available at *Brain* online.

References

Adzhubei IA, Schmidt S, Peshkin L, Ramensky VE, Gerasimova A, Bork P, et al. A method and server for predicting damaging missense mutations. Nat Methods 2010; 7: 248–9.

Ashokkumar B, Vaziri ND, Said HM. Thiamin uptake by the human-derived renal epithelial (HEK-293) cells: cellular and molecular mechanisms. Am J Physiol Renal Physiol 2006; 291: F796–805.

Debs R, Depienne C, Rastetter A, Bellanger A, Degos B, Galanaud D, et al. Biotin-responsive basal ganglia disease in ethnic Europeans with novel SLC19A3 mutations. Arch Neurol 2010; 67: 126–30.

den Dunnen JT, Antonarakis SE. Nomenclature for the description of human sequence variations. Hum Genet 2001; 109: 121–4.

Jhala SS, Hazell AS. Modeling neurodegenerative disease pathophysiology in thiamine deficiency: consequences of impaired oxidative metabolism. Neurochem Int 2011; 58: 248–60.

Koboldt DC, Chen K, Wylie T, Larson DE, McLellan MD, Mardis ER, et al. VarScan: variant detection in massively parallel sequencing of individual and pooled samples. Bioinformatics 2009; 25: 2283–5.

Kono S, Miyajima H, Yoshida K, Togawa A, Shirakawa K, Suzuki H. Mutations in a thiamine-transporter gene and Wernicke's-like encephalopathy. N Engl J Med 2009; 360: 1792–4.

Ku CS, Naidoo N, Pawitan Y. Revisiting Mendelian disorders through exome sequencing. Hum Genet 2011; 129: 351–70.

Leegwater PA, Vermeulen G, Konst AA, Naidu S, Mulders J, Visser A, et al. Subunits of the translation initiation factor eIF2B are mutant in leukoencephalopathy with vanishing white matter. Nat Genet 2001a; 29: 383–8.

Leegwater PA, Yuan BQ, van der Steen J, Mulders J, Konst AA, Boor PK, et al. Mutations of MLC1 (KIAA0027), encoding a putative membrane protein, cause megalencephalic leukoencephalopathy with subcortical cysts. Am J Hum Genet 2001b; 68: 831–8.

Li H, Durbin R. Fast and accurate short read alignment with Burrows-Wheeler transform. Bioinformatics 2009; 25: 1754–60.

Powers JM, de Vivo DC. Peroxisomal and mitochondrial disorders. In: Graham DI, Lantos PL, editors. Greenfield's neuropathology. New York: Arnold Press; 2002.

Rajgopal A, Edmondnson A, Goldman ID, Zhao R. SLC19A3 encodes a second thiamine transporter ThTr2. Biochim Biophys Acta 2001; 1537: 175–8.

Said HM, Balamurugan K, Subramanian VS, Marchant JS. Expression and functional contribution of hTHTR-2 in thiamin absorption in human intestine. Am J Physiol Gastrointest Liver Physiol 2004; 286: G491–8.

Scheper GC, van der Klok T, van Andel RJ, van Berkel CG, Sissler M, Smet J, et al. Mitochondrial aspartyl-tRNA synthetase deficiency causes leukoencephalopathy with brain stem and spinal cord involvement and lactate elevation. Nat Genet 2007; 39: 534–9.

Schiffmann R, van der Knaap MS. Invited article: an MRI-based approach to the diagnosis of white matter disorders. Neurology 2009; 72: 750–9.

Serrano M, Rebollo M, Depienne C, Rastetter A, Fernandez-Alvarez E, Muchart J, et al. Reversible generalized dystonia and encephalopathy from thiamine transporter 2 deficiency. Mov Disord 2012; 27: 1295–8.

Steenweg ME, Ghezzi D, Haack T, Abbink TE, Martinelli D, van Berkel CG, et al. Leukoencephalopathy with thalamus and brainstem involvement and high lactate 'LTBL' caused by EARS2 mutations. Brain 2012a; 135: 1387–94.

Steenweg ME, Vanderver A, Ceulemans B, Prabhakar P, Regal L, Fattal-Valevski A, et al. Novel infantile-onset leukoencephalopathy with high lactate level and slow improvement. Arch Neurol 2012b; 69: 718–22.

van der Knaap MS, Breiter SN, Naidu S, Hart AA, Valk J. Defining and categorizing leukoencephalopathies of unknown origin: MR imaging approach. Radiology 1999; 213: 121–33.

van der Knaap MS, Valk J. Magnetic resonance of myelination and myelin disorders. Heidelberg: Springer; 2005.

Wang K, Li M, Hakonarson H. ANNOVAR: functional annotation of genetic variants from high-throughput sequencing data. Nucleic Acids Res 2010; 38: e164.

Yamada K, Miura K, Hara K, Suzuki M, Nakanishi K, Kumagai T, et al. A wide spectrum of clinical and brain MRI findings in patients with SLC19A3 mutations. BMC Med Genet 2010; 11: 171.

Zara F, Biancheri R, Bruno C, Bordo L, Assereto S, Gazzerro E, et al. Deficiency of hyccin, a newly identified membrane protein, causes hypomyelination and congenital cataract. Nat Genet 2006; 38: 1111–13.

Zeng WQ, Al-Yamani E, Acierno JS Jr, Slaugenhaupt S, Gillis T, MacDonald ME, et al. Biotin-responsive basal ganglia disease maps to 2q36.3 and is due to mutations in SLC19A3. Am J Hum Genet 2005; 77: 16–26.

Zhao R, Gao F, Goldman ID. Reduced folate carrier transports thiamine monophosphate: an alternative route for thiamine delivery into mammalian cells. Am J Physiol Cell Physiol 2002; 282: C1512–17.

Zhao R, Gao F, Wang Y, Diaz GA, Gelb BD, Goldman ID. Impact of the reduced folate carrier on the accumulation of active thiamin metabolites in murine leukemia cells. J Biol Chem 2001; 276: 1114–18.